Understanding High-Speed Aeroelastic Stability of Swept-Tip Tiltrotor Blades

Xavier M. Delgado* and Anubhav Datta†
University of Maryland, College Park, Maryland 20742
and
Seyhan Gul‡
NASA Ames Research Center, Moffett Field, California 94035

https://doi.org/10.2514/1.C038396

A 4.75-ft-diameter, dynamically scaled, swept-tip proprotor was tested up to 200 kts. The stability roots (frequencies and damping) were collected for wing-pylon beam, chord, and torsion motions. The impacts of both gimbaled and gimbal-locked hubs were measured. Predictions from an in-house rotor aeromechanics solver were compared with data to understand the stability behavior and identify gaps in prediction capabilities. The data showed that swept-tip blades increased the damping of the wing chord and torsion modes, but only when the gimbal was locked through perturbation of hub pitch and roll moments. There was no significant effect on the beam mode. The comprehensive analysis was able to predict the stability trends generally, except for torsion, particularly when the gimbal was locked.

I. Introduction

THERE is a deficiency in aeroelastic stability data for swept-tip proprotor blades and a lack of validation of analytical tools, resulting in a gap in the fundamental understanding of their behavior. To address this gap, a 4.75-ft-diameter, dynamically scaled, swept-tip proprotor was tested in the Glenn L. Martin Wind Tunnel up to 200 kts with swept-tip proprotor blades. The model was installed on the Maryland Tiltrotor Rig (MTR) [1–3]. The MTR is specially designed to carry interchangeable blades, hubs, and wing spars to test advanced concepts. The only other test on swept-tip blades was reported in Ref. [3], which was also on the MTR, except that it was carried out in a Navy tunnel and was limited to 100 kts. This paper extends that work into the high-speed domain up to 200 kts, or 458 kts at full scale. Quantifying whirl-flutter stability at such unprecedentedly high speeds is necessary to realize jet-like cruise for tiltrotors. Additionally, a comprehensive rotor aeromechanics solver is used to predict the measured data and gain a fundamental understanding by comparison.§

Tiltrotors are versatile aircraft that combine the hover capability of a helicopter with the cruise capability of an airplane. Currently, cruise speeds are limited to 275–300 kts because of a combination of factors, the most critical of which is an instability known as tiltrotor whirl flutter. Tiltrotor whirl flutter is caused by interactions between large flexible rotors needed for flight and the flexible wing-pylon. Perturbations in the rotor motion cause perturbations in hub loads, resulting in wing motions that feed back into the rotor hub, closing the cycle. Innovations are needed in hubs, blades, and wings to mitigate whirl flutter and increase cruise speeds beyond 450 kts. Introducing blade sweep near the tip would be beneficial at high speeds because it would avoid compressibility drag from a high helical Mach number; therefore, understanding and characterizing the aeroelastic stability of swept-tip blades become important.

There is a rich history of tiltrotor testing and development. One of the earliest documented tiltrotors was the Bell Model 200, more commonly known as the XV-3. The XV-3 was originally plagued with instabilities, including whirl flutter, leading to several crashes [4,5]; however, these were not well understood at the time, as there was a lack of fundamental understanding and a deficiency in predictive capabilities [6]. Extensive full-scale testing of the XV-3 at the NACA Ames 40-ft-by-80-ft wind tunnel (now NASA Ames) was crucial for fully realizing a fundamental understanding during the 1950s and 1960s. Ultimately, the XV-3 proved that tiltrotors were viable candidates for Vertical Takeoff and Lift (VTOL) aircraft and led to the development of the XV-15. The success of the wind tunnel tests also demonstrated the value of testing, leading to full-scale and model-scaled tiltrotor testing campaigns. The former included semispan models like the Bell Model 300 [7], a 25-ft-diameter gimbaled rotor, and the Boeing Model 222 [8], a 26-ft-diameter hingeless hub. Both were tested in the 40-ft-by-80-ft wind tunnel during the early 1970s, along with full-scale testing of the XV-15. Unfortunately, the full-scale tests had limited data. The model-scaled tests were completed in parallel at other facilities in the U.S. Boeing built several models, including a 1/4.6 Froude-scale model of a tiltrotor [9], the M301 [10], and the M222 [11]. Only the model in Ref. [9] included stability data (blade frequency and damping vs RPM), but no flutter data. Bell built 1/5th-scale models of the V-22 and tested them at NASA Langley's Transonic Dynamics Tunnel from 1983 to 1987 [12]. There was also the Wing and Rotor Aeroelastic Test System (WRATS) [13], a derivative of the 1/5th-scale V-22 model, which included stability tests. These wind tunnel models also have absent or incomplete aeroelastic stability data. Regardless, the culmination of Bell's and Boeing's tiltrotor tests led to the successful development of the Bell Boeing V-22. More importantly, wind tunnel testing proved impactful and led to continued tiltrotor testing, which now makes public data a major focus.

Today, there are four major tiltrotor rigs: 1) NASA Tiltrotor Test Rig (TTR) [14,15]; 2) University of Maryland Tiltrotor Rig (MTR) [2,16,17]; 3) Army Tiltrotor Aeroelastic Stability Testbed (TRAST) [18,19]; and 4) Royal Netherlands Aerospace Center (NLR) Advanced Testbed for Tiltrotor Aeroelastic (ATTILA) [20,21]. The NASA TTR is a full-scale rig based on the Bell 609 rotor and is for performance and loads only. The other three are capable of testing aeroelastic stability and are smaller, model-scale, semispan wing-pylon rotor systems. All models have so far tested straight blades, except for one test on the MTR [3], which went up to 100 kts

Presented as Paper 2025-0428 at the AIAA SciTech 2025 Forum, Orlando, FL, January 6–10, 2025; received 23 January 2025; accepted for publication 2 January 2026; published online 20 March 2026.

*Graduate Research Assistant, Alfred Gessow Rotorcraft Center; delgadx2@umd.edu. Student Member AIAA (Corresponding Author).

†Professor, Alfred Gessow Rotorcraft Center; datta@umd.edu. Associate Fellow AIAA.

‡Research Engineer, Science and Technology Corporation, NASA Ames Research Center. Member AIAA.

§Distribution Statement A. Approved for public release; distribution is unlimited.

(229 kts at full scale) and measured only beam and chord damping. This work repeats test data up to 200 kts (458 kts at full scale) for beam, chord, and torsion damping to quantify the stability of the wing modes at high speeds, where whirl flutter is likely. Since whirl flutter is an instability that involves the rotor modes interfering with the wing modes, the stability is adequately quantified by the damping of the three wing modes.

There is substantial literature on the testing of advanced blade tips on helicopter rotors (see Ref. [22] for a summary), but only one measured aeroelastic stability. The 7.5-ft-diameter Advanced Dynamic Model rotor test by the U.S. Army at the Ames Research Center's 7-ft-by-10-ft tunnel measured the stability of swept-tip helicopter rotors [23]. There is less work on advanced blade tips on tiltrotors. The XV-15 was equipped with advanced technology blades that included swept-tip blades, but they were tested only for hover performance [24]. The French ONERA tested swept-tip blades on a model rotor for whirl flutter; however, there are few parametric data available, and the swept tip had both forward and aft sweep meant for improving aeroacoustics, not dynamics [25,26]. The objective of this research was to bridge this gap. Test data and predictions on swept-tip proprotor stability were recently published in our conference papers [27,28]. This paper summarizes the key results of both.

The paper begins with an overview of the MTR. This is followed by a description of the blades, wind tunnel testing, and signal processing for data extraction. An in-house comprehensive analysis, the University of Maryland Advanced Rotorcraft Code Version 2 (UMARC-II), is used to assess the data and gain insight into the fundamental mechanism [29–31]. The comprehensive analysis is described next. Finally, the data are presented in a parametric sequence.

II. MTR Overview

The MTR is a three-bladed semispan model with interchangeable hubs, blades, and spars. The blades and spar are loosely Froude-scaled to the starboard wing and rotor of the XV-15 aircraft. The present rotor has a radius of 2.375 ft (0.7239 m), which is a 1/5.26-scale of the XV-15. The rotor is electrically driven by a water-cooled permanent-magnet motor (Plettenberg NOVA 30). The motor has a maximum continuous power of 22 HP, a maximum torque of 59 ft · lb, and a maximum rotational speed of 5000 RPM. The nominal rotational speed for testing is 1050 RPM at Froude scale, which is 17.5 Hz and is defined as the once-per-revolution (or 1/rev) frequency. The hub is gimbaled, and the blades are straight and twisted as on the actual aircraft, but the gimbal can be locked with a custom plate as shown in Fig. 1, a unique feature of the model. The swept-tip blades share the same properties as the straight blades except for a 20 deg sweep starting from 80% rotor radius (R). The blades also have a twist of −37 deg over the span of the blade. The rotor frequencies are shown in Table 1 and are calculated using measured blade mass and stiffness properties. A departure from the XV-15 is in the lag frequency, which is much stiffer on the MTR than on the actual aircraft. The torsion frequency is very stiff on both and is unavailable. Another departure from the XV-15 is in the wing thickness: the MTR has an 18% thickness-to-chord ratio, which is much thinner than the 23% XV-15 wing. The frequencies of the wing were measured for the MTR and are shown in the same table. The beam and chord mode frequencies are similar to those of the XV-15 in./rev because of dynamic scaling. The torsion frequency is lower than that of the XV-15 because of the inertia of the slip ring, electric motor, and load cell within the pylon. The pylon center of gravity (C.G.) is also shifted 0.23 ft (0.07 m, 9.7% R) behind the wing spar because of these components. Three Ultramotion A2

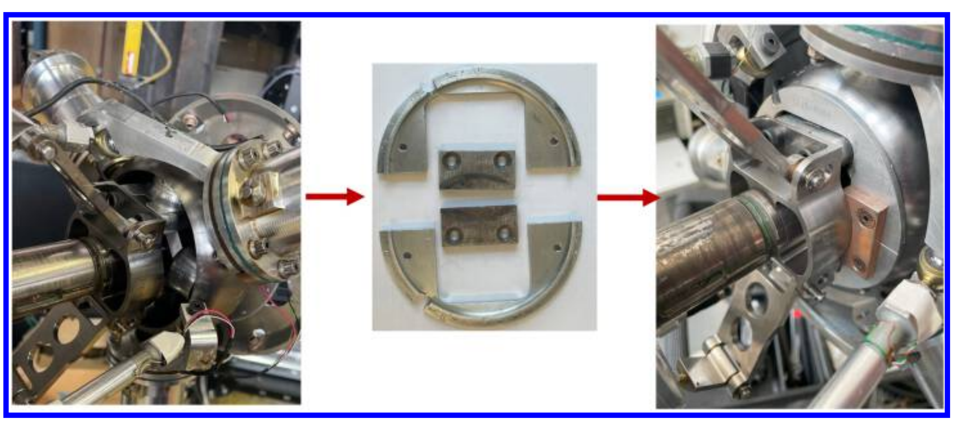

Fig. 1 Photograph of the MTR custom gimbal-locking plate (left to right: free gimbal, plate and fastening brackets, and locked gimbal).

Table 1 MTR properties

Variable	Unit	Value	Variable	Unit	Value
Radius	ft	2.375	⋮	⋮	⋮
Rotor speed	RPM	1050	Rotor frequencies:		
δ_3	deg	−15	Coll flap ν_{β_0}	/rev	1.79
Pylon C.G.	——	$-0.097R$	Cyclic flap ν_β	/rev	1.05
Pylon mass	lb	71.16	Lag ν_ζ	/rev	5.08
Pylon I_{PX}	lb·in.^{2}	4285	Wing frequencies:		
Pylon I_{PY}	lb·in.^{2}	4404	Beam: ω_b	/rev	0.29
Hub		Lockable gimbal	Chord: ω_c	/rev	0.55
Wing airfoil		NACA 0018	Torsion: ω_t	/rev	0.82
Blade airfoil		Boeing-vertol VR-7	Structural damping:		
Wing chord	in.	15.45	Beam: ζ_b	%	0.4
Blade chord	in.	3.15	Chord: ζ_c	%	1.3
⋮	⋮	⋮	Torsion: ζ_t	%	2.0

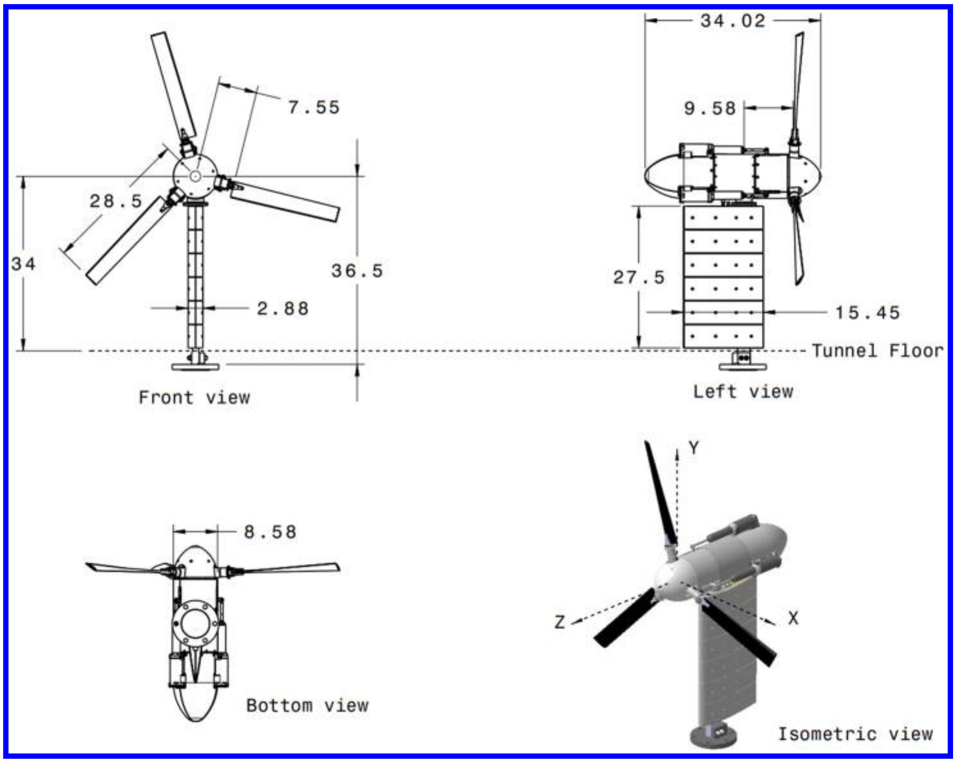

Fig. 2 Three-view diagram of the Maryland Tiltrotor Rig (dimensions are in inches).

linear servo actuators are used to perturb the model. The full stroke length is 3.75 in., giving approximately 55 deg of collective range. The actuators' maximum peak-to-peak pitch inputs for beam, chord, and torsion perturbations are 5.4, 2, and 0.1 deg, respectively. The actuation frequencies are 0.55/rev, 0.55/rev, and 0.82/rev, which respectively correspond to the wing beam, chord, and torsion frequencies. The MTR properties are summarized in Table 1. Figure 2 shows a three-view diagram with key dimensions.

III. Swept-Tip Blades

A planform view of the swept-tip blade is shown in Fig. 3. The blade has a span of 21 in., starting from 7.5 in. outboard of the hub center ($0.26R$ root cutout), providing a disk radius (R) of 28.5 in. The baseline (straight) blades have the same geometry except for the 20 deg sweep introduced at $0.8R$. The blade twist remains the same as that of the straight blades, -37 deg$/R$. The VR-7 airfoils have a 3.15 in. chord and are set along the swept axis. The blades are made of a ± 45 deg plainly woven IM7/8552 carbon-fiber prepreg fabric.

Figure 4 shows an exploded view of the blade components, without the spar and skin. The leading-edge foam follows the VR-7 airfoil profile up to $0.33c$ and is 15.3 in. long. The root of the leading-edge foam has material removed to accommodate the root insert. Seven tungsten weights lie along the leading edge of the foam and are spaced evenly along its length, from 0.26% R to 0.8% R. The trailing-edge foam keeps the remainder of the blade geometry, including the swept portion that begins at 80% R. Figure 5 shows the blade components assembled without the skin. There is

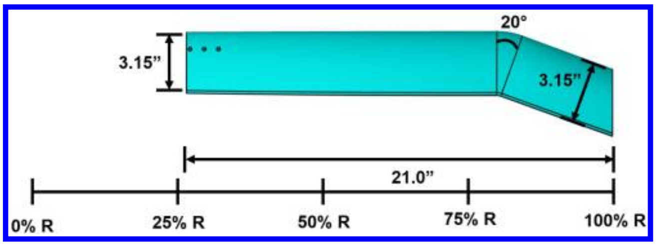

Fig. 3 Swept-tip blade CAD geometry.

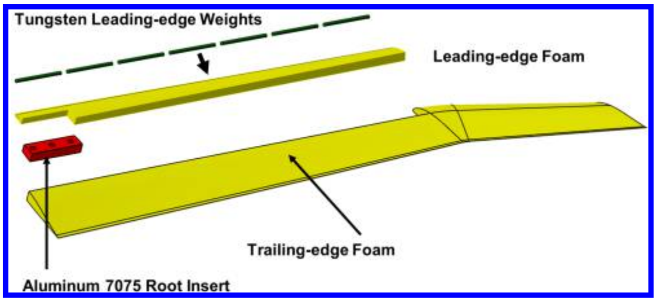

Fig. 4 Exploded view of swept-tip blade components (skin and spar not shown).

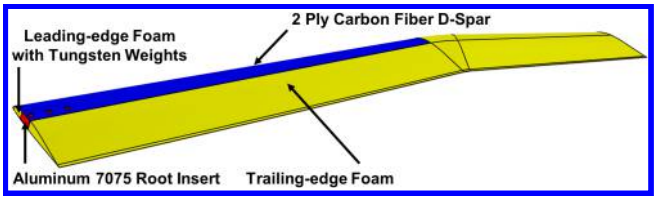

Fig. 5 Swept-tip blade with internal components assembled (skin not shown).

a 2-ply carbon-fiber (IM7/8552) D-spar in the straight portion, which terminates before the sweep begins. The blade features a 1-ply carbon-fiber (IM7/8552) skin with a specially cut tip that maintains the ± 45 deg ply layup along the swept section, preventing composite-material couplings. The final blade is pictured with a root grip adapter, for mounting to the MTR hub, in Fig. 7. The three blade masses used for the test were measured and are 171.03, 173.64, and 174.19 g.

Fabrication of the swept-tip blades follows Ref. [16], except for one deviation. The number of blade leading-edge weights is increased from five to seven, and the dimensions from 3.5 mm in diameter by 63 mm in length to 4 mm by 50 mm. Refining the leading-edge weights was an attempt to move the cross-sectional center of gravity forward while keeping the overall mass the same.

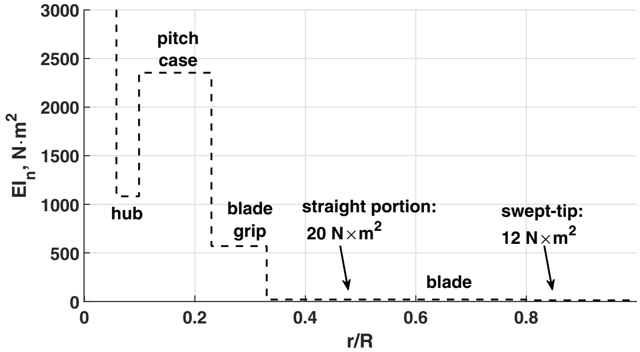

a) Beamwise stiffness

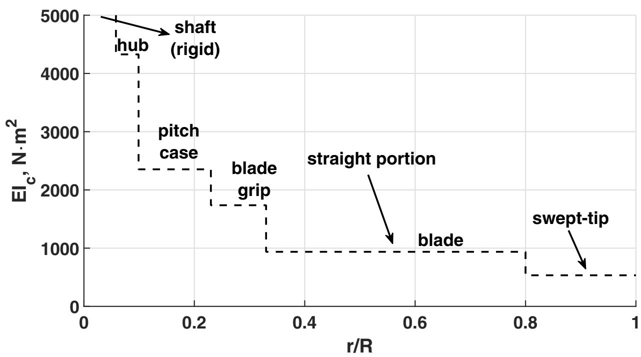

b) Chordwise stiffness

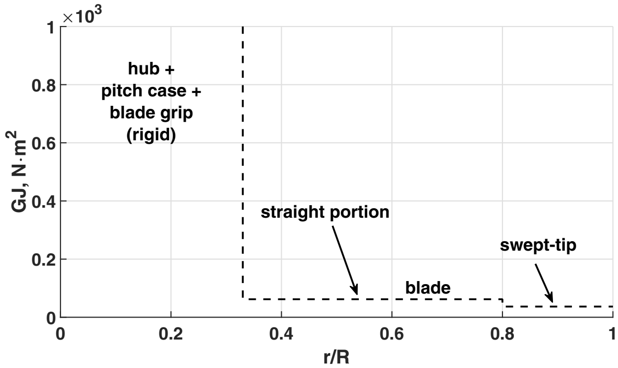

c) Torsional stiffness

Fig. 6 Structural stiffness properties for swept-tip blades.

The mass per unit length is 0.33 kg/m in the straight section and 0.15 kg/m in the swept section. The cross-sectional stiffnesses are shown in Fig. 6 in the normal, chord, and torsion directions.

IV. Wind Tunnel Testing

The Maryland Tiltrotor Rig (MTR) installed in the Glenn L. Martin Wind Tunnel is shown in Fig. 8. The clearance between the test floor and rotor tip is 8 in. ($0.28R$), which is slightly greater than the clearance between the rotor tip and the fuselage on the XV-15 aircraft ($0.1R$ or so).

The Glenn L. Martin Wind Tunnel has an 11.04 by 7.75 ft test section. The center of the test section has a 0.125 in. boundary-layer displacement thickness, which is insignificant compared to the tip

Fig. 7 Fabricated swept-tip blade.

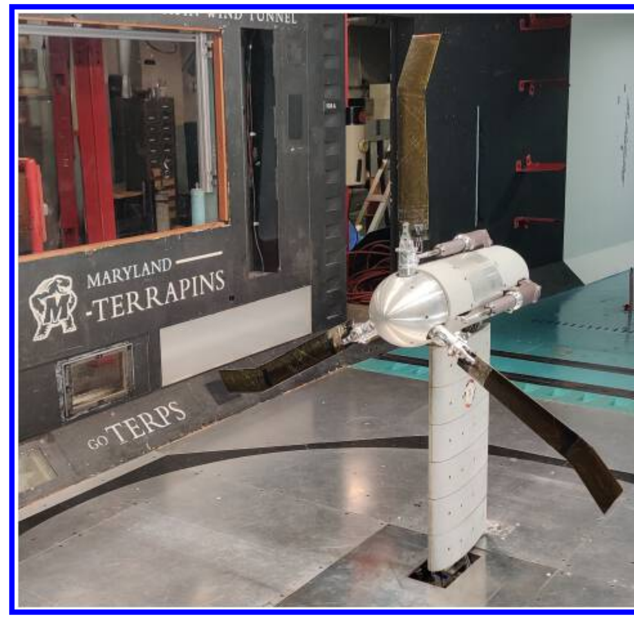

Fig. 8 Swept-tip blades installed on MTR at the Glenn L. Martin tunnel.

Table 2 Flutter test conditions: freewheeling and wing on

Sweep no.	Speed, kts	Collective, θ_{75}, deg	Rotation rate, RPM	Gimbal
Straight blades				
U1	30–100	10–40	1050	Locked
U2	30–180	10–55	1050	Locked
U3	30–193	10–58	1050	Free
Swept-tip blades				
U4	30–190	10–57	1050	Free
U5	30–200	10–58	1050	Locked
U6	100	36–54	700–1400	Locked

clearance. The minimum and maximum airspeeds are 30 and 200 kts, respectively, with corresponding freestream Mach numbers 0.045–0.3. The test section turbulence factor is 1.05, implying that the effective Reynolds number is 1.05 times that of the model Reynolds number. The measured hot-wire intensity is 0.21%, which indicates very low turbulence levels.

The test matrix consisted of six cases, as given in Table 2. The cases are designated $U1$–$U6$. $U1$–$U5$ are speed sweeps at a constant RPM and are the subject of this paper. $U6$ was an RPM sweep at constant speed and will not be discussed in this paper. $U1$–$U3$ were conducted with straight blades, and $U4$–$U6$ were conducted with swept-tip blades. Within each sweep, a test point is identified by its principal variable. For example, the test point $U3.193$ would mean that the 193 kts condition of the $U3$ sweep.

The test procedure was similar to the straight-blade tests given in Ref. [32]. The algorithms used to extract damping were also identical, but the software implementation was refined to filter out frequencies well outside the expected range. Filtering removes rotor harmonics and noise, minimizing scatter in the data. The extraction methods are discussed in Sec. VI.

V. Signal Processing

The MTR has three high-bandwidth electric actuators that can perturb the model below the swashplate at a specified frequency. The perturbation frequencies are the natural frequencies of the wing beam, chord, and torsion modes. Strain gauges on the spar record the time history. The beam and chord modes are 14% of the wing-span up from the base; however, the beam gauge is centered on the upper and lower surfaces of the spar, and the chord gauges are centered on the leading and trailing edges of the spar. The torsion

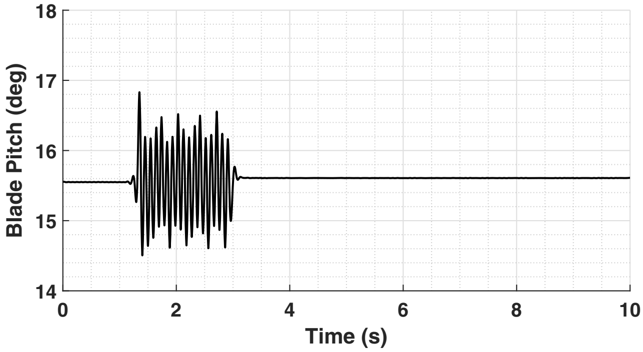

Fig. 9 Sample perturbation input as read by blade pitch measurements.

gauges are placed at 18% of the wingspan and are centered on the upper and lower surfaces of the spar. The wingspan of the MTR is 34.25 in. Each mode is excited at least three times with significant pauses in between to let the dynamics reach steady state. All time histories are approximately 10 s long and consist of an initial steady state before perturbation (2 s), ramp (1 s of perturbation), free response, and a decay to steady state. The perturbation input within the ramp state is effectively sinusoidal Heaviside, as shown in Fig. 9. The frequency and damping are extracted from the strain data in the free-response segment.

First, the data are downsampled from 10 to 1 kHz to reduce the computational effort, except for the torsion mode. The torsion mode decayed quickly, and it was not downsampled so as to use all data points available. Next, the data were band-pass filtered to remove frequencies not within ±2 Hz of the expected frequency. The expected frequencies for each wing mode (Table 1) are measured before flutter testing with a resonance assessment profile (RAP) test. Figure 10 shows sample beam, chord, and torsion signals before and after filtering. Finally, the damping is extracted using either moving-block or Prony, as described in Sec. VI.

VI. Damping Extraction

Two methods are used to extract the damping: moving-block and Prony. The moving-block method is applicable for low damping ratios, typically less than 5% critical. Prony's method applies to all damping ratios.

Moving-block effectively smooths the signal by taking a moving average, which makes it resistant to noisy signals. The moving-block method consists of three main steps: selecting a window and block size, computing the fast Fourier transform (FFT) of the signal within the block, and moving the block over in time. Here, a boxcar window is selected. Consider the filtered beam signal in Fig. 10b, redrawn in Fig. 11 to show the three portions of the signal: steady state (preperturbation), ramp (perturbation), and decay (postperturbation). The moving-block method is illustrated in Fig. 12. A bit-sized (2^n) sample window is taken from the decay portion. Figure 12a shows a 4096-size sample window. The window in Fig. 12a is expanded in Fig. 12b. Within the window, a block size of 1024 is moved in time until the entire window is traversed. Figure 12b also shows the block at three different positions—at the start, after 1600 samples, and at the end. At each position, an FFT is taken, as shown in Fig. 12c. The peak amplitude is stored along with the corresponding damped frequency, ω_d. The natural logarithm of the peak amplitude for each block is plotted against time in Fig. 12d. A linear regression is applied, and the slope of the line is equal to $-\zeta\omega_n$, where ζ is the damping ratio and ω_n is the natural frequency. Assuming ($\omega_d \approx \omega_n$), the damping ζ is found.

Prony's method reconstructs a signal as a sum of M damped sinusoids. Each mode has an amplitude, frequency, damping ratio, and phase. The order of the method, M, is related to the number of modes needed for the best fit. The relationship between M and the fitting error is nonlinear; therefore, increasing the order does not necessarily reduce the error of the fit for a noisy signal. Figure 13 shows Prony fits for two orders. The accuracy of the fit is determined by the slope, S, and coefficient of determination, R^2—these are used to select the best order for Prony's method. Here, $M = 125$, is the more accurate of the two. In Fig. 14, the triangles mark the linear fit for $M = 125$, and the circles mark the linear fit for $M = 1000$. A frequency spectrum is made for the best fit by sorting the amplitudes by frequency. The maximal amplitude, within an expected frequency range, is selected, and the corresponding frequency and damping ratio are stored.

VII. Comprehensive Analysis

Predictions from a comprehensive analysis are used to establish a fundamental understanding of the aeroelastic phenomenon. A comprehensive rotor analysis brings together structural models, aerodynamic models, trim, and flutter solution procedures for a rotary-wing system [33]. In this work, the University of Maryland Advanced Rotorcraft Code Version 2 (UMARC-II) is used as the baseline platform [29,30,34]. A diagram of the model is shown in Fig. 15.

The structure is modeled using 1-D Euler–Bernoulli beam finite elements. The elements are assumed isotropic and include 15 degrees of freedom in flap, lag, torsion, and extension. The blades have a symmetric ±45 deg layup, and hence this level of modeling is adequate. The wing spar is also isotropic. There are 18 elements for each blade and 12 elements for the wing-pylon-hub—8 for the wing, 3 for the pylon, and 1 for the hub shaft. The pitch horn and swashplates were modeled through boundary conditions and element connectivity. Structural properties of the wing, pylon, and blades are measured in-house [16,35]. Structural damping is measured before every test, and this value is input directly.

The aerodynamics are modeled using C81 airfoil decks and unsteady lifting-line theory. The airfoil decks are generated using in-house CFD and include tables of airfoil c_l, c_d, and c_m about the quarter-chord ($1/4c$) for angles of attack ±180 deg and Mach numbers up to 0.85. The rotor (VR-7) has seven aerodynamic panels. Radial-flow corrections are applied. Freewake was an option, but it was observed not to make any difference in the result, as the high-speed conditions quickly wash away the wake of the rotor [29]. So, uniform induced inflow was adequate, although even a zero induced inflow would produce the same results. The wing (NACA 0018) has 14 aerodynamic panels.

UMARC-II can calculate stability in two ways: 1) eigenanalysis or 2) time-marching. In eigenanalysis, the rotor degrees of freedom are converted to multiblade coordinates in the fixed frame. The mass, damping, and stiffness matrices are calculated by perturbing them from the trim solution, from which eigenvalues are determined. The eigenvalues yield the frequencies and damping ratios of the modes. Eigenanalysis is the preferred method for cases beyond instability. In time-marching, the control angles are perturbed exactly as in the test, and the decay history is used to extract damping. A two-point backward Euler scheme is used. The numerical damping is first calculated from an identical case with no aerodynamic or structural damping. The numerical damping is subtracted from the calculated damping later. Both solution procedures must produce the same results when the structure is stable, and this is verified in Fig. 16, which shows the beam damping calculated with either method for an arbitrary case. The eigenanalysis and time-marching results are also the same for chord and torsion damping, but only the beam is shown. Predictions are artificially limited to 200 kts, the maximum speed capable in the wind tunnel, so as to maintain the scope of validating predicted data.

VIII. Collective Versus Speed

The freewheeling condition (unpowered air-driven rotation) typically produces an earlier flutter boundary. Powered flight is also representative of the turboshaft engine drive, which is difficult to scale and, hence, not part of the model. The results in this paper are all in the freewheeling condition. In freewheeling, the rotor is

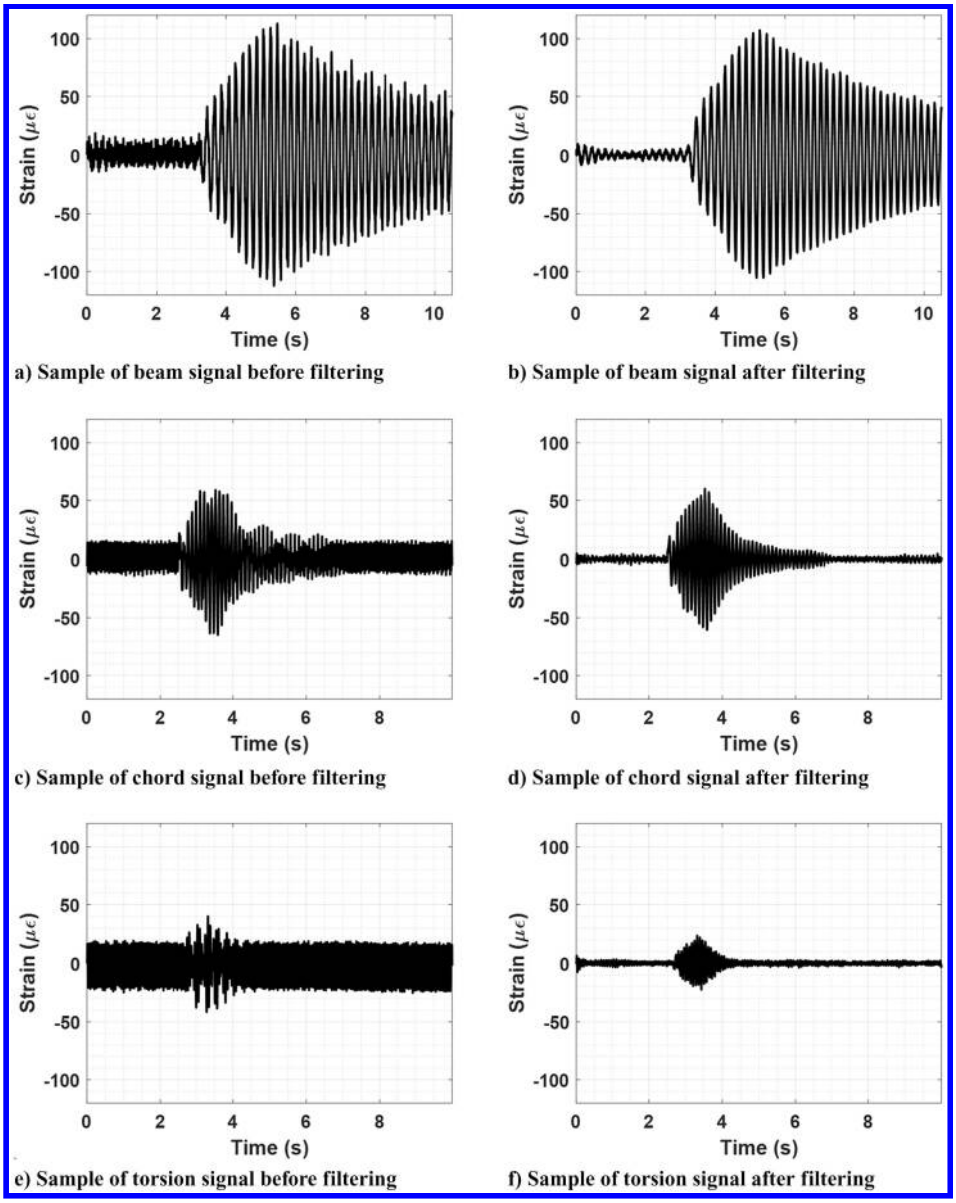

Fig. 10 Sample of beam, chord, and torsion signals before and after filtering; test point U4.50.

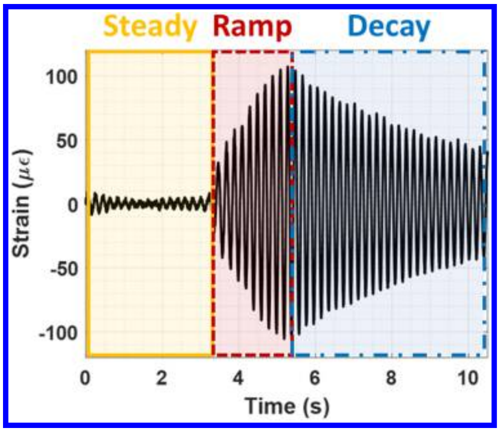

Fig. 11 The perturbation response of the beam mode signal; test condition *U*4.50.

trimmed to the nominal rotation speed—1050 RPM for Froude-scale testing of this rotor—by controlling the collective, θ_{75}. When the rotor is gimbaled, once-per-revolution cyclic inputs are used to limit the first-harmonic flapping. Although the MTR is tested in axial flow conditions, blade flapping is still present because of residual imbalances; hence, there is a need to trim.

The collective is measured using three-pitch encoders, one for each blade. The swept-tip blade collectives are shown with predictions for the gimbaled rotor in Fig. 17. Predictions for the gimbal-locked rotor are shown in Fig. 18. Only the collectives of blades 2 and 3 are shown because blade 1 had a sensor loss. For the gimbal-locked rotor, blade 2 also had a sensor loss after 140 kts. UMARC-II is able to predict the collectives well. After the trim solution is achieved, perturbations are applied through the swashplate via high-bandwidth electric actuators to excite the three wing modes one by one.

IX. Swept-Tip Blades with a Gimbaled Hub

After the perturbations end, the signal decay is analyzed to extract the frequency and damping ratio. The wing-pylon frequencies are shown in Fig. 19. There is no appreciable change in frequency with blades or hub type; therefore, frequency plots are not repeated. The wing mode frequencies are easy to predict, as shown by the solid lines in Fig. 19, and they match the data. The blade frequencies were not measured; hence, predictions were not included.

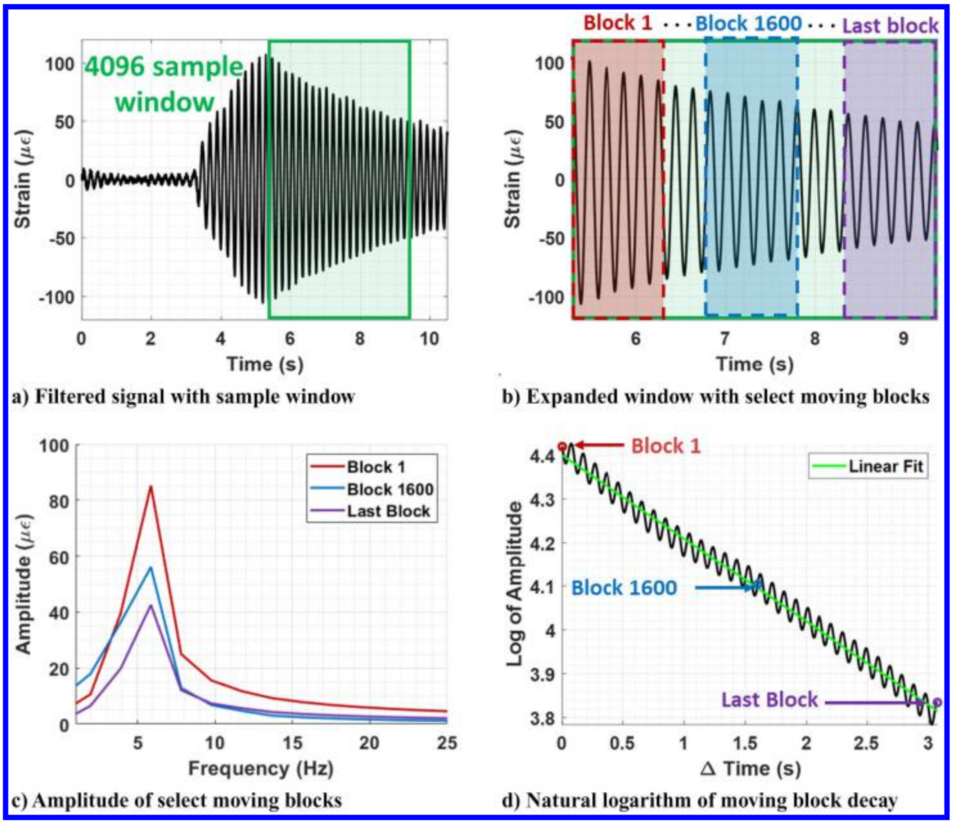

a) Filtered signal with sample window
b) Expanded window with select moving blocks
c) Amplitude of select moving blocks
d) Natural logarithm of moving block decay

Fig. 12 Moving-block method applied to the beam signal; test point *U*4.50.

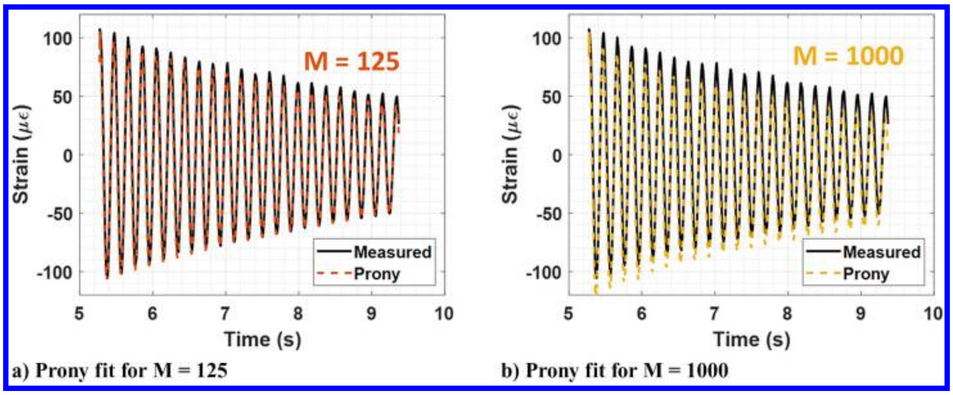

a) Prony fit for M = 125
b) Prony fit for M = 1000

Fig. 13 Prony reconstruction of beam signal; test point *U*4.50.

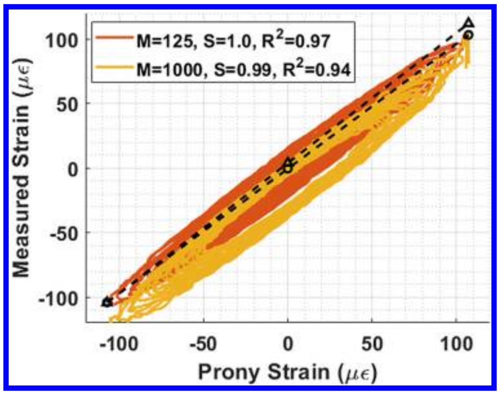

Fig. 14 Measured signal versus Prony fit for $M = 125$ and $M = 1000$; test point *U*4.50.

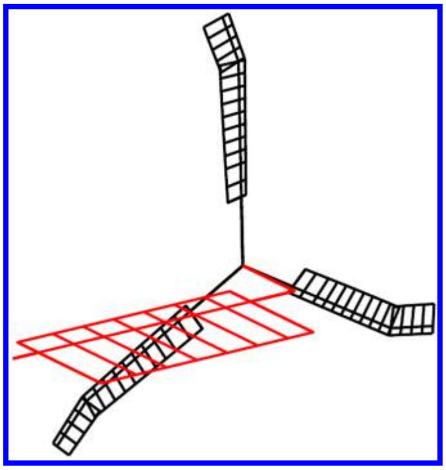

Fig. 15 UMARC-II model representation.

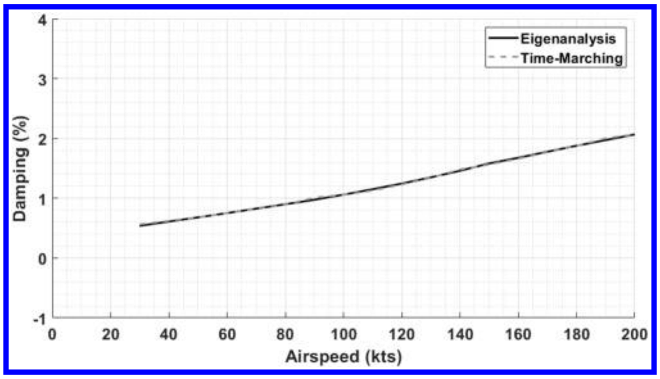

Fig. 16 Beam damping results comparing eigenanalysis versus time-marching.

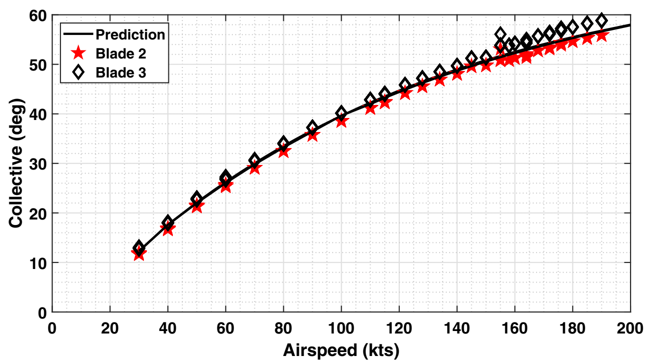

Fig. 17 Collective versus airspeed; gimbal free; test sweep *U*4.

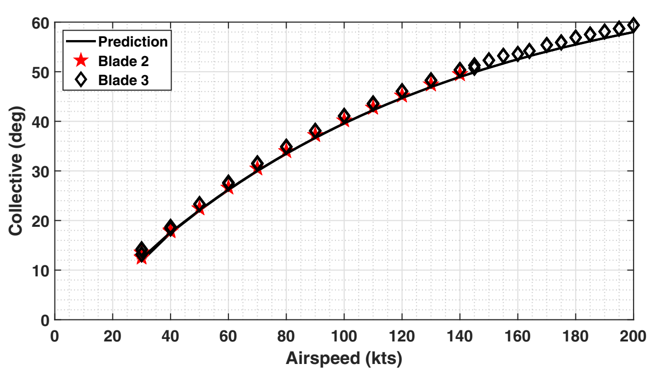

Fig. 18 Collective versus airspeed; gimbal locked; test sweep *U*5.

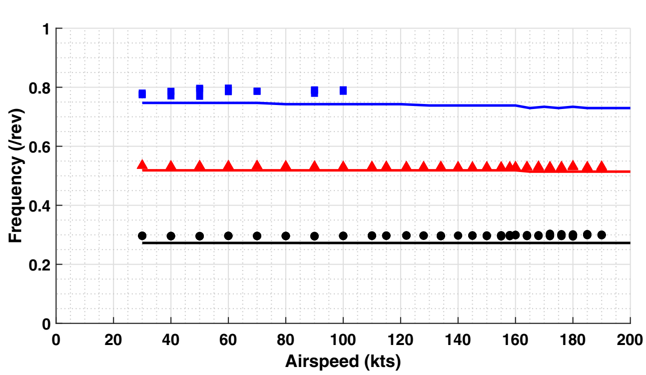

Fig. 19 Nondimensional frequencies versus airspeed. Rotor speed 1050 RPM (17.5 Hz).

The damping of the wing modes is plotted versus airspeed in Fig. 20. Each speed consists of three trials, and all three are shown to quantify the scatter.

At 30 kts, the beam damping is approximately 0.5% and generally increases linearly by approximately 0.1% every 10 kts. There is also scatter beyond 100 kts, which is not unexpected for such high speeds. Predictions show the same trend, with perhaps one exception. The damping decreases from 180 kts, which is not captured by the predictions, although the trend is not clear enough for a strong conclusion.

The chord damping also shows a linear trend like the beam mode, except now there is a decrease in the damping. The predictions capture the trend, although not as sharply. At low speeds, the damping is slightly underpredicted, whereas at high speeds it is slightly overpredicted. The chord mode has approximately 2% damping at 30 kts, but this is reduced to 1.25% by 190 kts. The reduction here is about −0.5% damping for every 10 kts. There also appears to be a drop above 180 kts, which is not captured by the predictions.

The torsional damping is unlike the beam and chord modes because now the trend is nonlinear with airspeed. The torsional

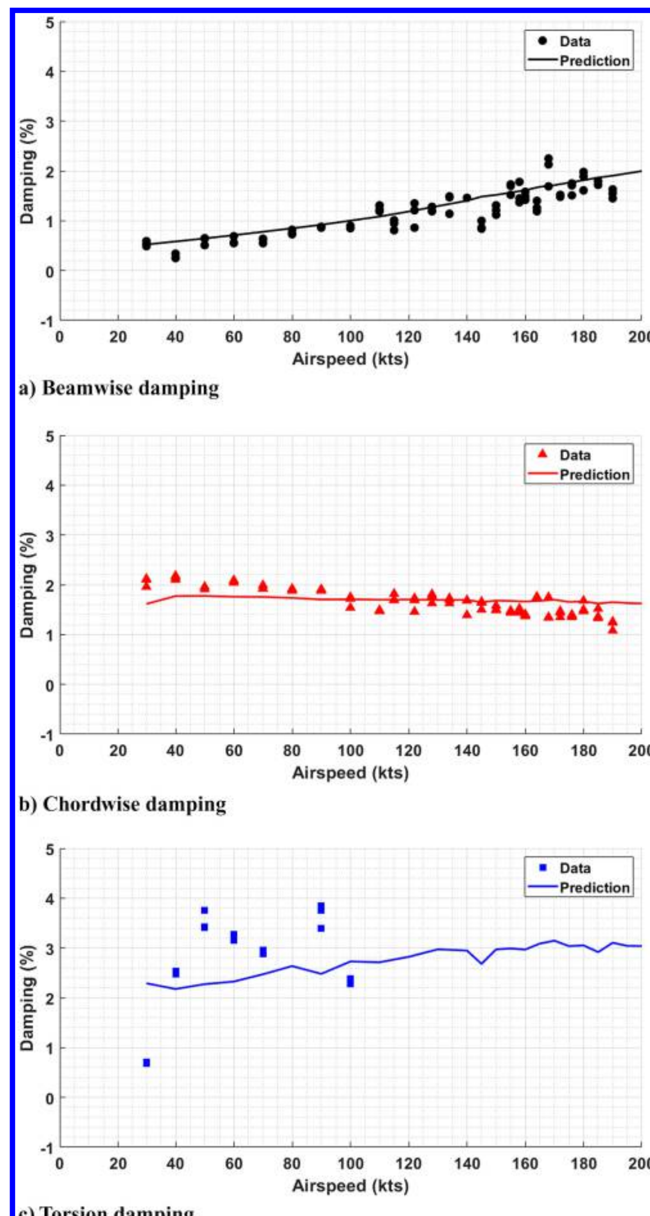

Fig. 20 Wing mode damping ratio versus airspeed for swept-tip blades and gimbal-free hub.

damping is 1% critical at 30 kts and rises quickly to 4% critical at 50 kts. After 50 kts, the torsion damping decreases and peaks again around 90 kts before decreasing again. Predictions are poor in general, although in the same range as the data (1–3%).

Perturbing torsion was difficult beyond 100 kts because of the low signal-to-noise ratio. The high damping in torsion compromises the moving-block method; thus, it is compared to the Prony method in the subsequent section.

X. Moving-Block Versus Prony

A key limitation of the moving-block method is the assumption that the damped frequency is approximately equal to the natural frequency ($\omega_d = \omega_n\sqrt{1-\zeta^2} \approx \omega_n$). The assumption typically begins to break down as damping reaches 5% or higher. As such, moving-block is compared to the Prony method to verify the damping measurements.

Figure 21a shows that the moving-block and Prony methods are in agreement for the beam mode, although Prony shows slightly less scatter. The drop in damping near 200 kts is also confirmed by Prony when comparing the beam data. Figure 21b shows similar results for chord. Figure 21c shows that the two methods have the maximum discrepancy, as expected, but still have fair agreement. Both methods confirm a nonlinear trend in torsion damping. Moving-block and Prony match for all cases, but Prony shows less scatter; therefore, only Prony is shown henceforth for brevity.

XI. Gimbal-Free Versus Gimbal-Locked Hub

Now the gimbal is locked. This produces a stiff-in-plane hingeless hub. Comparisons are drawn between the two hub configurations using the speed sweep numbers $U4$ and $U5$ in Table 2.

The beam damping is shown in Fig. 22a. The damping is comparable, though there is a slight increase in damping with the gimbal locked at lower speeds. Locking the gimbal appears to decrease beam mode stability slightly. Predictions capture the trend, although the damping is underestimated at speeds less than 60 kts.

The chord damping is shown in Fig. 22b. The gimbal-locked chord damping increased markedly between 80 and 160 kts from 2 to 3% but remains around 3% on average. The predictions are unable to capture the increase. The predictions show some rise in damping when the gimbal is locked, but not as dramatic. The difference is not from the locking plate, which adds friction and dissipates energy. Any damping in the locking plate would increase

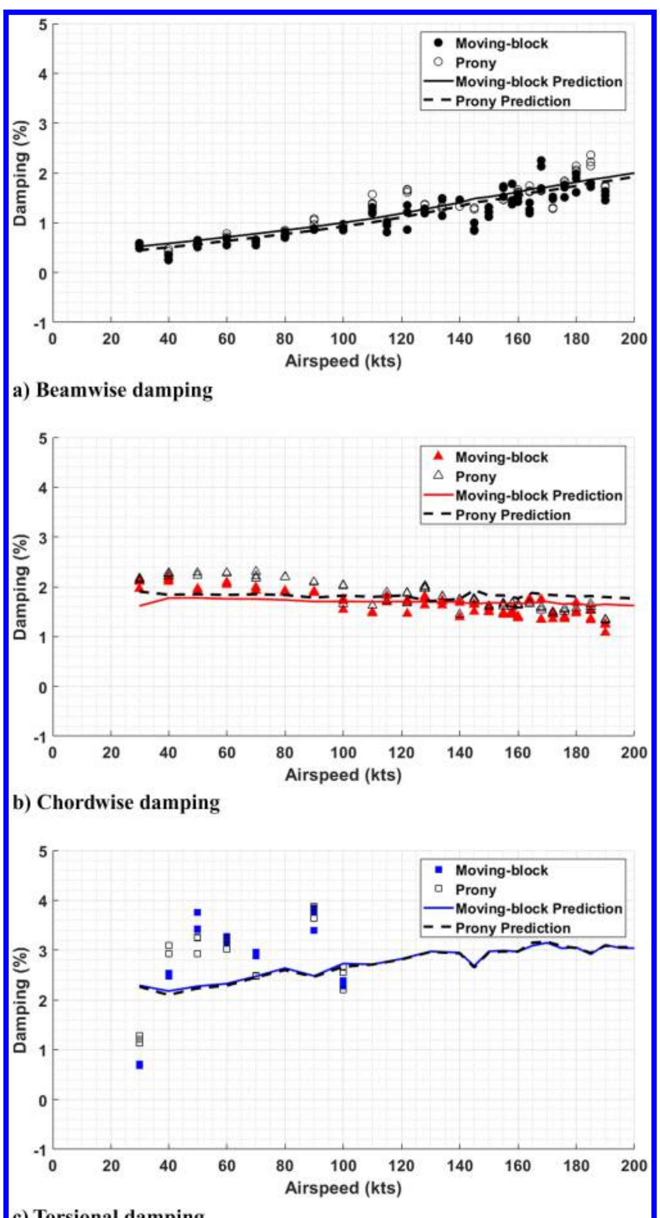

Fig. 21 Wing mode damping versus airspeed with comparison of moving-block and Prony methods.

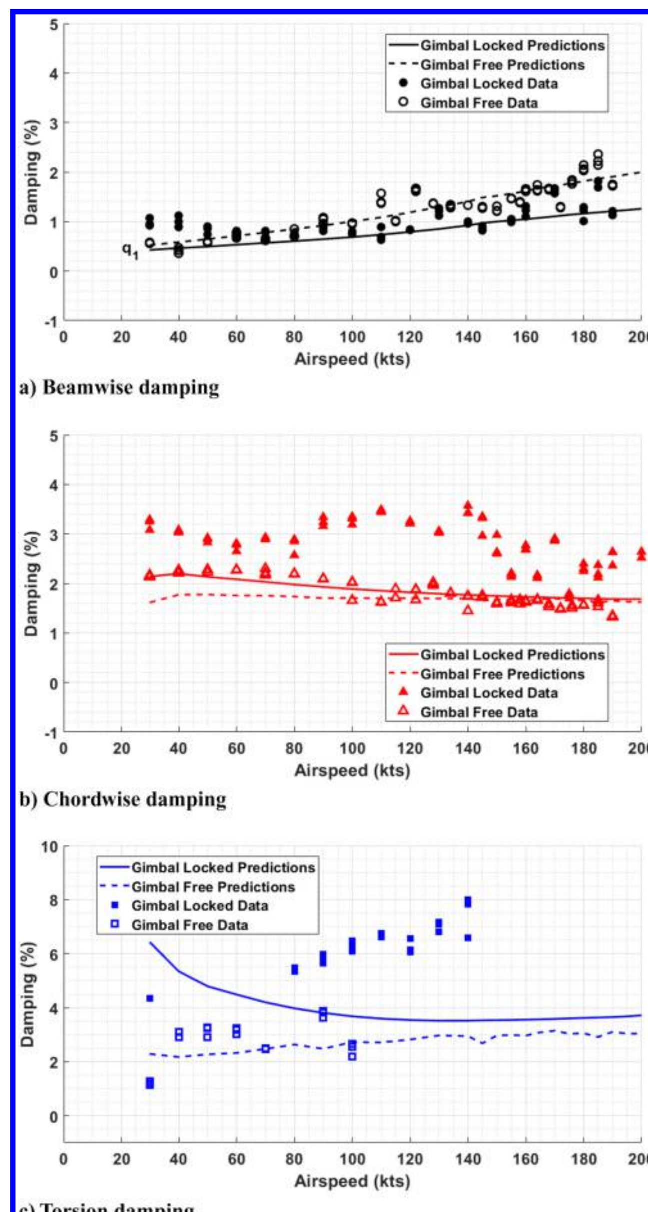

Fig. 22 Gimbal-free versus gimbal-locked hub; swept-tip blades with predictions.

the damping uniformly across speed regardless of aerodynamics; however, no such increase was measured in structural damping.

Torsional damping is compared in Fig. 22c. Neither the trend nor the magnitude is predicted. Even at the lowest speed, 30 kts, gimbal-locked predictions show more than three times the measured damping. Between 40 and 70 kts, the torsion mode could not be excited. At 80 kts, the damping is 5% and linearly increases to 8% at 130 kts. There is also a slight drop in damping at 115 kts. Predictions fail to capture the trends, whereas the data show a clear linear increase in damping; the predictions show an asymptotic decrease. Overall, the gimbal-free predictions are at least similar in trend and magnitude, whereas there is a clear discrepancy with the gimbal-locked predictions.

In summary, the beam damping is mostly unaffected by locking the gimbal and remains easy to predict. The chord and torsion damping increase significantly. The chord damping increases uniformly at all speeds. The torsion appears to increase linearly with speed. UMARC-II has difficulty predicting these modes. Even though the precise reason is unclear, eigenvector analysis reveals significant coupling in these modes: torsion and chord in lag and beam, chord, and lag in torsion.

The discrepancy of the gimbal-locked torsion mode warranted an exploration of the eigenvectors to gain some insights. The eigenvector for the wing beam mode at 200 kts is shown in Fig. 23, with the x-axis and y-axis being the real and imaginary planes, respectively. No scale is shown because it is only their relative magnitudes that are relevant. The eigenvectors for a given mode rotate counterclockwise at the damped frequency, and the magnitudes decrease exponentially by the damping ratio. Figure 23 shows that the beam mode is dominated by the transverse beam displacement, q_1, as expected. There is negligible coupling between the beam mode and other wing or rotor modes. The resulting mode shape for q_1 is shown in red within Fig. 24 along with the initial system at rest in grayscale.

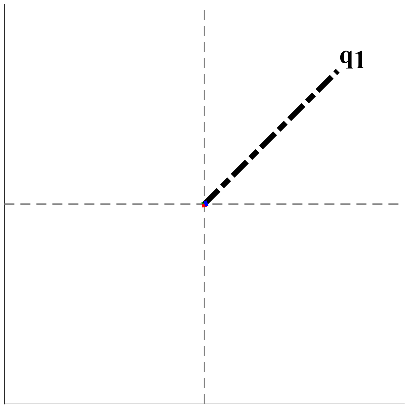

Fig. 23 Eigenvector on complex plane showing modal participation for beam mode, q_1, at 200 kts.

Fig. 24 First beam-bending mode shape of wing-pylon at 200 kts.

The eigenvector for the chord mode at 200 kts, Fig. 25, shows that the wing chordwise displacement, q_2, dominates. There is also minor coupling with the wing twist, p, and the blade's fixed-frame lateral lag motion, ζ_{1S}. Overall, the chord mode eigenvector is describing a system that induces a rotor roll moment and wing twisting when perturbed in the chordwise direction. The mode shape for q_2 is shown in Fig. 26 along with the initial resting position.

The torsion mode eigenvector at 200 kts is depicted in Fig. 27. Here there is a significant contribution from the beam mode, as well as from longitudinal lag, ζ_{1C}, collective lag, ζ_0, and chord mode, q_2. The contributions are not easy to see from only the mode shape in Fig. 28; hence, the eigenvector plot is important. This does not reveal the source of the discrepancy but clarifies that the torsion mode is more complicated than the beam or chord modes and requires accurate predictions of all contributing motions.

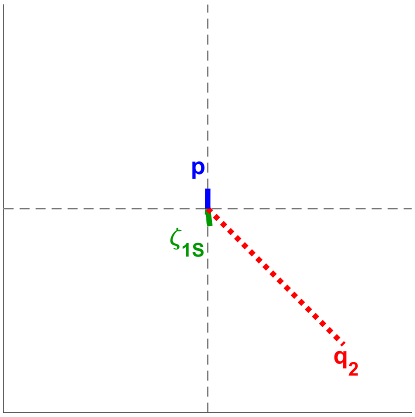

Fig. 25 Eigenvector on complex plane showing modal participation for chord mode, q_2, at 200 kts.

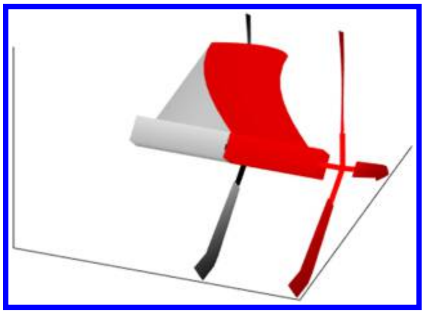

Fig. 26 First chord-bending mode shape of wing-pylon at 200 kts.

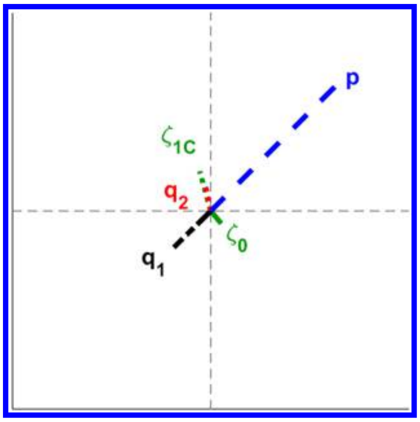

Fig. 27 Eigenvector on complex plane showing modal participation for torsion mode, p, at 200 kts.

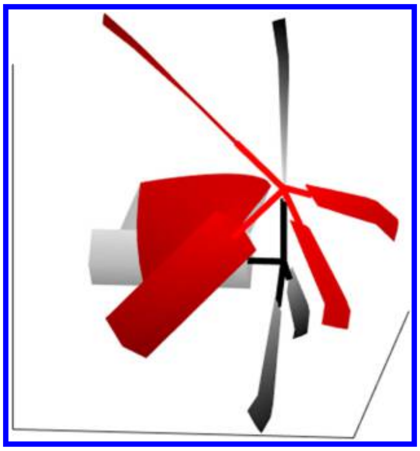

Fig. 28 First torsion mode shape of wing-pylon at 200 kts.

XII. Swept-Tip Versus Straight Blades

In Ref. [32], the authors had earlier reported results from straight blades (sweep numbers $U1$–$U3$). This section compares the straight-blade results with the new swept-tip results.

The stability of the gimbaled hub model is shown in Fig. 29. The data are from sweep numbers U3 and U4. Figure 29a shows the beam damping. The swept-tip blades show no significant effect on the beam damping when comparing the data (Fig. 29a). Perhaps there is a slight decrease in damping below 80 kts, but the predictions are indistinguishable from each other. The data appear to show a slightly higher increase with speed, crossing over perhaps 120 kts, but predictions show no such trends.

Figure 29b shows the chord damping. Perhaps there is a slight increase in damping below 80 kts, but the predictions are once again indistinguishable from each other. The data appear to show a slightly higher decrease with speed, crossing over perhaps around 120 kts, but predictions show no such trends. In contrast to a beam, the chord damping does not change significantly with speed.

Figure 29c shows torsion damping. The predictions indicate that the swept-tip blades should generally have lower damping, at least at speeds below 150 kts, but the lack of overlapping data prevents a firm conclusion. Like the data, the predictions also show the discontinuous behavior in damping, both from moving-block and Prony, so it is not a numerical artifact. Overall, the torsion predictions show only a gross agreement with the data, but there is clearly more to understand about the torsion stability.

The stability of the gimbal-locked hub model is shown in Fig. 30. The data are from sweep numbers $U3$ and $U4$. The beam data, Fig. 30a, show a slight decrease in stability with swept-tip blades. Predictions show a similar effect. Predictions also indicate that the straight blades show a faster increase with airspeed. The reduction in stability with swept-tip is small but appears to grow with speed.

Figure 30b shows chord stability. Measured data show sweep increases chord stability, but predictions show a slight decrease.

Figure 30c shows torsion stability. Data show an increase in damping with speed for the swept-tip blades. As before, predictions show the highest discrepancy in torsion. They are unsatisfactory both in magnitude and trends, although the effect of increased damping is seen.

The effect of sweep enters through the nonzero hub pitch and yaw moments (M_Y and M_X in Fig. 2), which appear when the gimbal is locked and transfer to the wing. The pitch affects the torsion, and the yaw affects the chord. The beam mode is not affected by the hub moments but rather by the vertical force (F_X in Fig. 2; H-force in rotorcraft terminology). Locking the gimbal changes blade flapping motion, which affects the vertical force.

XIII. Conclusions

A 4.75-ft-diameter, dynamically scaled, swept-tip proprotor was tested in a wind tunnel for aeroelastic stability up to 200 kts

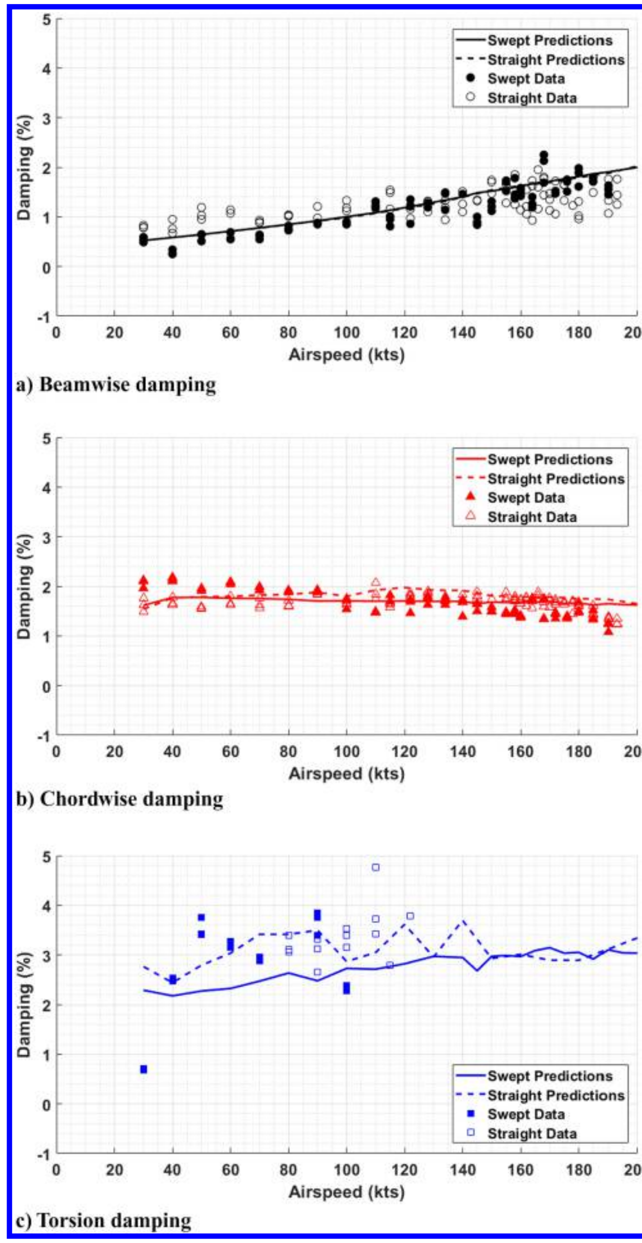

Fig. 29 Gimbal free damping versus airspeed; straight versus swept blades.

(equivalent to 450 kts in full scale). The effect of hub type—gimbaled and gimbal-locked—was also measured. The damping of swept blades was compared to straight blades. The model was loosely scaled to the XV-15 tiltrotor. Stability roots were measured at a Froude-scale RPM of 1050. The stability roots consisted of frequency and damping of the beam, chord, and torsion wing-pylon modes. An in-house rotor aeromechanics analysis was carried out to compare with test data. The following key conclusions are drawn from this work:

1) Swept-tip blades do not show a significant effect on wing damping, at least at the Froude-scale tip speeds.

2) Swept-tip blades increased chord and torsion damping when the gimbal was locked. Chord damping increased from 2% critical to approximately 3% critical between 80–160 kts. The torsion damping changed from a nonlinear trend with airspeed—fluctuating around 3% critical—to a linearly increasing trend with more than 5% critical damping above 80 kts.

3) In general, locking the gimbal had a dramatic impact on chord and torsion damping, but not on the beam damping. The chord damping generally increased by 50%. The torsion damping more than doubled at higher speeds.

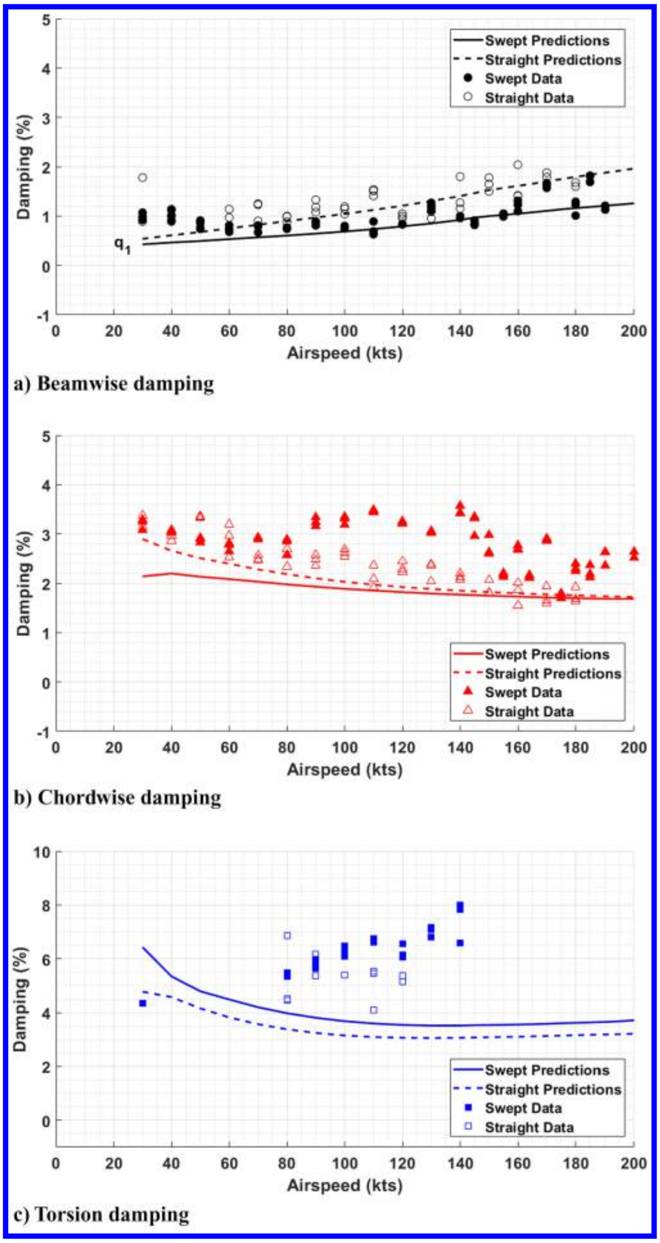

Fig. 30 Gimbal-locked damping versus airspeed; straight versus swept blades.

4) The effect of the sweep appears to enter through the hub moments, which appear when the gimbal is locked. The hub pitch moment affects the torsion mode, and the hub yaw affects the chord mode. The beam mode damping is unaffected by the hub moments.

5) No whirl flutter was encountered during testing.

6) Predictions were able to capture the stability trends generally; however, the gimbal-locked torsion prediction showed a significant discrepancy.

Future work will involve powered tests and a flutter-prone configuration to elucidate the effect of sweep near instability. The source of prediction discrepancies remains unknown; therefore, additional validation data are needed to deduce the underlying cause. As such, predictions will be repeated with the current UMARC-II version. The resulting data from future tests will be used to improve UMARC-II.

Acknowledgments

This work was carried out with the support of the Army, Navy, and NASA through the Vertical Lift Research Center of Excellence grant (no. W911W62120003) under Mahendra Bhagwat (Army) and technical monitoring from Tom Parham (Bell), William Welsh (Sikorsky), and Hyeonsoo Yeo (Army). We thank them for their insights and suggestions.

References

[1] Datta, A., Tsai, F., and Sutherland-Foggio, J., “Design of a New Tilt Rotor Test Facility at the University of Maryland,” *AIAA Scitech 2019 Forum*, AIAA Paper 2019-2136, 2019. https://doi.org/10.2514/6.2019-2136

[2] Tsai, F., Sutherland, J. R., Akinwale, A., Morin, A., Gul, S., and Datta, A., “Whirl Flutter Test of the Maryland Tiltrotor Rig: Overview,” *AIAA SCITECH 2022 Forum*, AIAA Paper 2022-0567, 2022. https://doi.org/10.2514/6.2022-0567

[3] Sutherland, J., Tsai, F., and Datta, A., “Whirl Flutter Test of Swept-Tip Tiltrotor Blades,” *Journal of the American Helicopter Society*, Vol. 69, No. 1, 2024, pp. 1–12. https://doi.org/10.4050/JAHS.69.012010

[4] Koenig, D. G., Greif, R. K., and Kelly, M. W., “Full-Scale Wind-Tunnel Investigation of the Longitudinal Characteristics of a Tilting-Rotor Convertiplane,” NASA SP 2000-4517, 1959.

[5] Koenig, D. G., Morelli, J. P., and Warmbodt, W. G., “Full-Scale Prop-Rotor Stability Tests on the XV3 at High Advance Ratios,” NASA TM 2015-21881, 2015.

[6] Maisel, M. D., Giulianetti, D. J., and Dugan, D. C., “The History of the XV-15 Tilt Rotor Research Aircraft from Concept to Flight,” NASA SP 2000-4517, 2000.

[7] Marr, R., Sambell, K., and Neal, G. T., “V/STOL Tilt Rotor Study. Volume VI: Hover, Low Speed and Conversion Tests of a Tilt Rotor Aeroelastic Model (Model 300),” NASA CR 114615, 1973.

[8] Magee, J., and Alexander, H., “Wind Tunnel Tests of a Full Scale Hingeless Prop/Rotor Designed for the Boeing Model 222 Tilt Rotor Aircraft,” NASA CR 114664, 1973.

[9] Magee, J., and Alexander, H., “Wind Tunnel Test on a 1/4.622 Froude Scale, Hingeless Rotor, Tilt Rotor Model,” NASA CR 151937, 1976.

[10] Ham, N., Bauer, P., Lawrence, T., and Yasu, M., “A Study of Gust and Control Response of Model Rotor-Propellers in a Wind Tunnel Airstream,” NASA CR 137756, 1975.

[11] Ham, N. D., and Whitaker, H. P., “A Wind-Tunnel Investigation of Tilt-Rotor Gust Alleviation Systems,” NASA CR 152264, 1978.

[12] Popelka, D., Sheffler, M., and Bilger, J., “Correlation of Test and Analysis for the 1/5-Scale V-22 Aeroelastic Model,” *Journal of the American Helicopter Society*, Vol. 32, No. 2, 1987, pp. 21–33. https://doi.org/10.4050/JAHS.32.21

[13] Piatak, D. J., Kvaternik, R. G., Nixon, M. W., Langston, C. W., Singleton, J. D., Bennett, R. L., and Brown, R. K., “A Parametric Investigation of Whirl-Flutter Stability on the WRATS Tiltrotor Model,” *Journal of the American Helicopter Society*, Vol. 47, No. 2, 2002, pp. 134–144. https://doi.org/10.4050/JAHS.47.134

[14] Acree, C., Sheikman, A. L., and Norman, T. R., “High-Speed Wind Tunnel Tests of a Full-Scale Proprotor on the Tiltrotor Test Rig,” *Vertical Flight Society 75th Annual Forum*, Vertical Flight Soc., Philadelphia, PA, 2019, pp. 1–19. https://doi.org/10.4050/F-0075-2019-14736

[15] Acree, C., “Vertical Climb Testing of a Full-Scale Proprotor on the Tiltrotor Test Rig,” *VFS Aeromechanics for Advanced Vertical Flight Technical Meeting*, Vertical Flight Soc., San Jose, CA, 2020, pp. 1–15.

[16] Sutherland, J. R., Tsai, F., and Datta, A., “Whirl Flutter Test of the Maryland Tiltrotor Rig: Swept-Tip Blades,” *AIAA SCITECH 2022 Forum*, AIAA Paper 2022-0568, 2022. https://doi.org/10.2514/6.2022-0568

[17] Gul, S., and Datta, A., “Whirl Flutter Test of the Maryland Tiltrotor Rig: Prediction and Validation,” *AIAA SCITECH 2022 Forum*, AIAA Paper 2022-0927, 2022. https://doi.org/10.2514/6.2022-0927

[18] Kreshock, A. R., Thornburgh, R., and Wilbur, M., “Overview of the TiltRotor Aeroelastic Stability Testbed,” *AIAA SCITECH 2022 Forum*, AIAA Paper 2022-0566, 2022. https://doi.org/10.2514/6.2022-0566

[19] Kreshock, A., Thornburgh, R., Wilbur, M., Kang, H., Piatak, D., and Sekula, M., “Initial Whirl-Flutter Characterization of the TiltRotor Aeroelastic Stability Testbed,” *Proceedings of the Vertical Flight Society 79th Annual Forum*, Vertical Flight Soc., West Palm Beach, FA, 2023, pp. 1–18. https://doi.org/10.4050/F-0079-2023-18037

[20] Van 'T Hoff, S., Van Vilsteren, J., Cocco, A., and Masarati, P., "Design of a Tiltrotor Semi-Span Wind Tunnel Model for Whirl Flutter Investigations," *AIAA SCITECH 2023 Forum*, AIAA Paper 2023-1306, 2023. https://doi.org/10.2514/6.2023-1306

[21] Montaño-Oliveros, J., Fonte, F., Van't Hoff, S., and Timmerman, B., "Whirl Flutter Analysis of a Tiltrotor Semi-Span Wind Tunnel Model for Test Results Correlation," *49th European Rotorcraft Forum 2023*, DGLR-Lilienthal-Oberth e.V., Bückeburg, 2023, pp. 1–17.

[22] Chi, C., Datta, A., Chopra, I., and Chen, R., "Three-Dimensional Strains on Twisted and Swept Composite Rotor Blades in Vacuum," *Journal of Aircraft*, Vol. 58, No. 1, 2021, pp. 1–16. https://doi.org/10.2514/1.C035746

[23] Maier, T. H., Sharpe, D. L., and Abrego, A. I., "Aeroelastic Stability for Straight and Swept-Tip Rotor Blades in Hover and Forward Flight," *American Helicopter Society 55th Annual Forum*, American Helicopter Society, Montréal, Québec Canada, 1999.

[24] Bartie, K., Alexander, H., McVeigh, M., Lamon, S., and Bishop, H., "Hover Performance Tests of Baseline Metal and Advanced Technology Blade (ATB) Rotor Systems for the XV-15 Tilt Rotor Aircraft," NASA CR 177436, Oct. 1986.

[25] Beaumier, P., Decours, J., and Lefebvre, T., "Aerodynamic and Aero-Acoustic Design of Modern Tilt-Rotors: The ONERA Experience," *26th International Congress of the Aeronautical Sciences*, ICAS Paper 2008-1.7.4, Sept. 2008.

[26] Krüger, W. R., "Multibody Analysis of Whirl Flutter Stability on a Tiltrotor Wind Tunnel Model," *Proceedings of the Institution of Mechanical Engineers, Part K: Journal of Multi-Body Dynamics*, Vol. 230, No. 2, 2016, pp. 121–133. https://doi.org/10.1177/1464419315582128

[27] Delgado, X., and Datta, A., "High Speed Whirl Flutter Tests of Swept-Tip Tiltrotor Blades," *AIAA SCITECH 2024 Forum*, AIAA Paper 2024-1851, 2024. https://doi.org/10.2514/6.2024-1851

[28] Delgado, X., and Datta, A., "High Speed Whirl Flutter Tests and Predictions of Swept-Tip Tiltrotor Blades," *AIAA SCITECH 2025 Forum*, AIAA Paper 2025-0428, 2025.

[29] Gul, S., and Datta, A., "Development of an Aeromechanics Solver for Loads and Stability of Hingeless Tiltrotors," *Journal of Aircraft*, Vol. 60, No. 1, 2023, pp. 143–159. https://doi.org/10.2514/1.C036944

[30] Gul, S., and Datta, A., "Aeroelastic Loads and Stability of Swept-Tip Hingeless Tiltrotors Toward High-Speed Instability-Free Cruise," *Journal of the American Helicopter Society*, Vol. 68, No. 1, 2023, pp. 1–18. https://doi.org/10.4050/JAHS.68.012001

[31] Gul, S., and Datta, A., "Prediction and Validation of Whirl Flutter Data of the Maryland Tiltrotor Rig," *Journal of the American Helicopter Society*, Vol. 69, No. 1, 2024, pp. 1–11. https://doi.org/10.4050/JAHS.69.012011

[32] Akinwale, A., and Datta, A., "High Speed Whirl Flutter Tests of the Maryland Tiltrotor Rig," *Vertical Flight Society 79th Annual Forum*, Vertical Flight Soc., West Palm Beach, FL, 2023, pp. 1–17. https://doi.org/10.4050/F-0079-2023-18035

[33] Johnson, W., "A History of Rotorcraft Comprehensive Analyses," NASA TP 2012-216012, April 2012.

[34] Gul, S., and Datta, A., "Fundamental Understanding and Prediction of Loads and Stability of a Full-Scale Hingeless Tiltrotor," *AIAA Scitech 2021 Forum*, AIAA Paper 2021-0090, 2021. https://doi.org/10.2514/6.2021-0090

[35] Sutherland, J., and Datta, A., "Fabrication, Testing, and 3D Comprehensive Analysis of Swept-Tip Tiltrotor Blades," *Journal of the American Helicopter Society*, Vol. 68, No. 1, 2023, pp. 1–17. https://doi.org/10.4050/JAHS.68.012002

J. Leishman
Associate Editor